Heterogeneous nucleation of creases in swelling polymer gels

Jianzhu Ju, Ken Sekimoto, Luca Cipelletti, Costantino Creton, Tetsuharu Narita

Heterogeneous nucleation of creases in swelling polymer gels

Jianzhu Ju [a], Ken Sekimoto [b,c], Luca Cipelletti [d,e], Costantino Creton [a,f], Tetsuharu Narita[*, a,f]

[a] Sciences et Ingénierie de la Matière Molle, CNRS UMR 7615, ESPCI Paris, PSL Université, Paris, France

[b] Gulliver, CNRS-UMR7083, ESPCI, 75231 Paris, France

[c] Matières et Systèmes Complexes, CNRS-UMR7057, Université Paris-Diderot, 75205 Paris, France

[d] Laboratoire Charles Coulomb (L2C), University of Montpellier, CNRS, Montpellier, France

[e] Institut Universitaire de France, Paris, France

[f] Global Station for Soft Matter, Global Institution for Collaborative Research and Education, Hokkaido University, Sapporo, Japan

Abstract

Surface creasing is a common occurrence in gels under strong enough compression. The transition from smooth to creased surface has been well-studied in equilibrium conditions and applied to achieve stimuli-responsive properties. Classical predictions of the creased state, assuming the gel is at equilibrium and homogeneous, are generally satisfactory, while the transient behavior in swelling gels is often far from equilibrium and is commonly heterogeneous. The short-time response is essential for materials in dynamic environments, but it remains unreported and largely unknown due to the limited temporal resolution of the techniques used so far. Here, we use spatially resolved multi-speckle diffusing wave spectroscopy (MSDWS) with sub-microsecond time resolution to measure the spatially dependent swelling and creasing of a constrained poly (vinyl alcohol) chemical gel in borax solutions of varying concentrations. Our high speed imaging by MSDWS shows that the swelling behavior and mechanical response at the microscopic level can be highly heterogeneous in time and space, and is detectable hundreds of seconds before the corresponding macroscopic creasing transition. This unprecedented visualization of the heterogeneous and time-dependent behavior beyond equilibrium morphological changes unveils the full complexity of the transient material response after exposure to external stimuli and sheds light on the formation mechanism of metastable states in transient processes.

[*]correspondence authors: tetsuharu.narita@espci.fr

I. Introduction

When a gel is under strong enough compression, periodical surface creasing (singular regions formed in a sharp folding) is commonly generated as the result of buckling instabilities, as schematically shown in **Fig. 1(a)** [1, 2]. The mathematical significance of the mechanical instability induced pattern has attracted many theoretical and experimental investigations aiming at understanding its topological nature [3, 4] and mechanical origins [2, 5-7]. Recently, the stimuli-responsive nature of surface buckling has been used advantageously to design a surface with tunable morphology and properties [8-10]. As creasing can be well controlled by different stimuli such as temperature [8, 11], external deformation [6, 12] and pH [13], the practical performance of the functionalized surface pattern is essentially limited by the time scale of the dynamic response when exposed to external stimuli [14, 15]. While for static conditions equilibrium models have successfully described the critical nucleation condition [16, 17] and growth kinetics of creasing [18], there are many open questions concerning the transient behavior during the creasing transition; in particular, the possible existence and life time of metastable states may be important for the design of properties and practical applications of the materials.

In a well-defined condition where the swollen gel film adheres to a rigid substrate, lateral deformation is limited by the substrate so that swelling leads to an equiaxial compression, which commonly causes surface creasing [2, 17]. Equilibrium models typically assume that the gel remains homogeneous and at mechanical equilibrium without stress gradients ($\partial\sigma/\partial x$ = 0) [19, 20]. With measurements of the crease morphology at the swelling equilibrium, the critical creasing condition can be related to the equilibrium swelling ratio α_∞ (ratio of final and initial weight of the gel) [5, 17, 21]. For creases generated during transient swelling, i.e. well before reaching α_∞ [2, 18, 22-24], the nucleation and growth of creases is considered to depend on swelling kinetics, which is only governed by cooperative diffusion of water [18, 25].

While at equilibrium experiments are in agreement with both theoretical analysis [11, 18, 21] and simulations [1, 5], the transient state before reaching equilibrium is rarely discussed. Remarkably, it has been reported that surface creasing is a subcritical process where the critical condition can deviate dramatically from equilibrium conditions due to energy barriers [26, 27], such as surface energy [5, 11], inelasticity [26, 28] and interactions with the substrate [29]. At the onset of creasing, the selective folding of the surface indicates the existence of structural frustration and heterogeneity before macroscopic creasing sets in, where local stability is sacrificed to benefit global stability. During the transient metastable state, the nucleation of creasing and the swelling kinetics may not be simply predicted by the quasi-static models [22, 30, 31]. The swelling and creasing kinetics are controlled by the equilibrium final state (α_∞), which itself changes with compression level [20, 32]. To gain insight into the creasing transition and the role of heterogeneity and transient kinetics, a method with both spatial and temporal resolution is required.

Multi-speckle diffusing wave spectroscopy (MSDWS) [33, 34] is an extension of conventional dynamic light scattering that detects the decorrelation of light multiply scattered by a small amount of probe particles embedded in the sample, providing a good tool to observe spatially and temporally resolved microscopic response during dynamic transitions [35, 36]. Here we apply MSDWS to investigate creasing in a relatively simple geometry, where creasing is induced during the one-dimensional (1D) swelling of a constrained hydrogel before reaching swelling equilibrium. A common strategy to tune the swelling ratio and kinetics is to adjust the cross-linker concentration. However, this inevitably changes significantly the initial elastic modulus [17, 21], thus modifying an important system parameter [21, 37]. In this work, swelling is induced and tuned by the introduction of charges in a neutral chemical gel by complexation. In-situ measurements with MSDWS shows that the creasing process during swelling contains a non-equilibrium nucleation period where swelling and creasing is spatially heterogeneous and deviates from the 1-D kinetics described by the diffusion equation, showing the existence of long-lived metastable states. Contrary to common knowledge, rich heterogeneous behaviors occur at different temporal/spatial scales, both before and during creasing, which cannot be detected with ordinary methods. Fast optical measurements by MSDWS supplements the imaging of the transient behavior during the generation of transient surface patterns, and provides a tool for the investigation of general dynamic processes.

II. Morphological observation

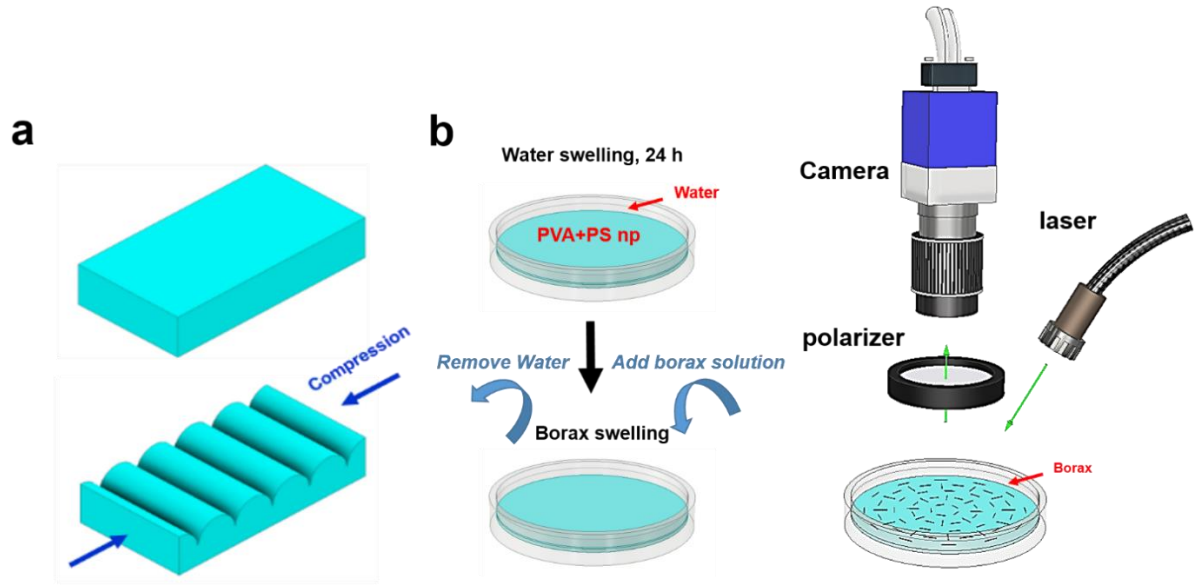

Fig. 1 *(a) Schematic of surface creasing in a compressed gel. (b) Sample preparation and in-situ measurement of constrained swelling.*

The preparation and the swelling of PVA chemical gels are described in **APPENDIX A**. To induce swelling, borax solutions with different concentration (C_b) are poured on the PVA chemical gels prepared in a petri dish (**Fig. 1(b)**). The initial thickness of the gel (H_0=1.85 mm) is much smaller than its radius (55 mm) and the gel adheres to the surface of the plastic petri dish, thus the gel swelling is one dimensional, along the thickness direction. Free swelling experiments were performed in parallel, where gels were taken out of the initial mold for crosslinking and immersed in the solutions. Swelling ratios α can be measured from the ratio of the measured weight m to the initial weight m_0, which for 1D swelling is also identical to the thickness ratio ($\alpha = \frac{m}{m_0} = \frac{H}{H_0}$). The equilibrium swelling ratios α_∞ of the constrained (1D swelling) and free (3D swelling) gels are compared in **Fig. 2(a)**. α_∞ increases with C_b and reaches a plateau for $C_b > 2$ mM for both constrained and free swelling. The plateau value for the constrained gels ($\alpha_\infty \approx 2.2$) is lower than that of the free-swelling gels ($\alpha_\infty \approx 3$). In constrained gels, periodically distributed streak-like creases can be observed over the whole sample surface for $C_b \geq 1.5$ mM (see pictures in **Fig. 2(a)**, with $C_b = 6$ mM before and after swelling for 2 days). During the swelling process, the sample is illuminated by non-polarized white light and surface images are collected with a CMOS camera. Images are subtracted from the initial image right after swelling to better visualize the creases. The creased region where the gel folds downwards reflects more light, so that creases appear as bright zones, as shown in **Fig. 2(b)**. Detectable creases appear between 600 and 800 s for C_b = 4 mM, and between 90 and 300 s for C_b = 10 mM. The spatial distribution of creases is initially not homogeneous, until they fill all the surface of the gel, after which an increase of the crease size over time can be observed. The evolution of the surface pattern formed by the ceases can be characterized by a characteristic length d [18, 21], defined as the average distance between creases. d is estimated by 2D FFT processing of the images (**APPENDIX B**) and plotted in **Fig. 2(c)**. Different growth kinetics are observed for solutions with different C_b, while the final length is similar, around 2 mm. d is of the order of the sample thickness and reaches plateau after long swelling time with similar value at different C_b. This matches well with the results that similar α_∞ values are measured for different C_b over 4 mm (**Fig. 2(a)**), in agreement with previously reported observations [18, 21].

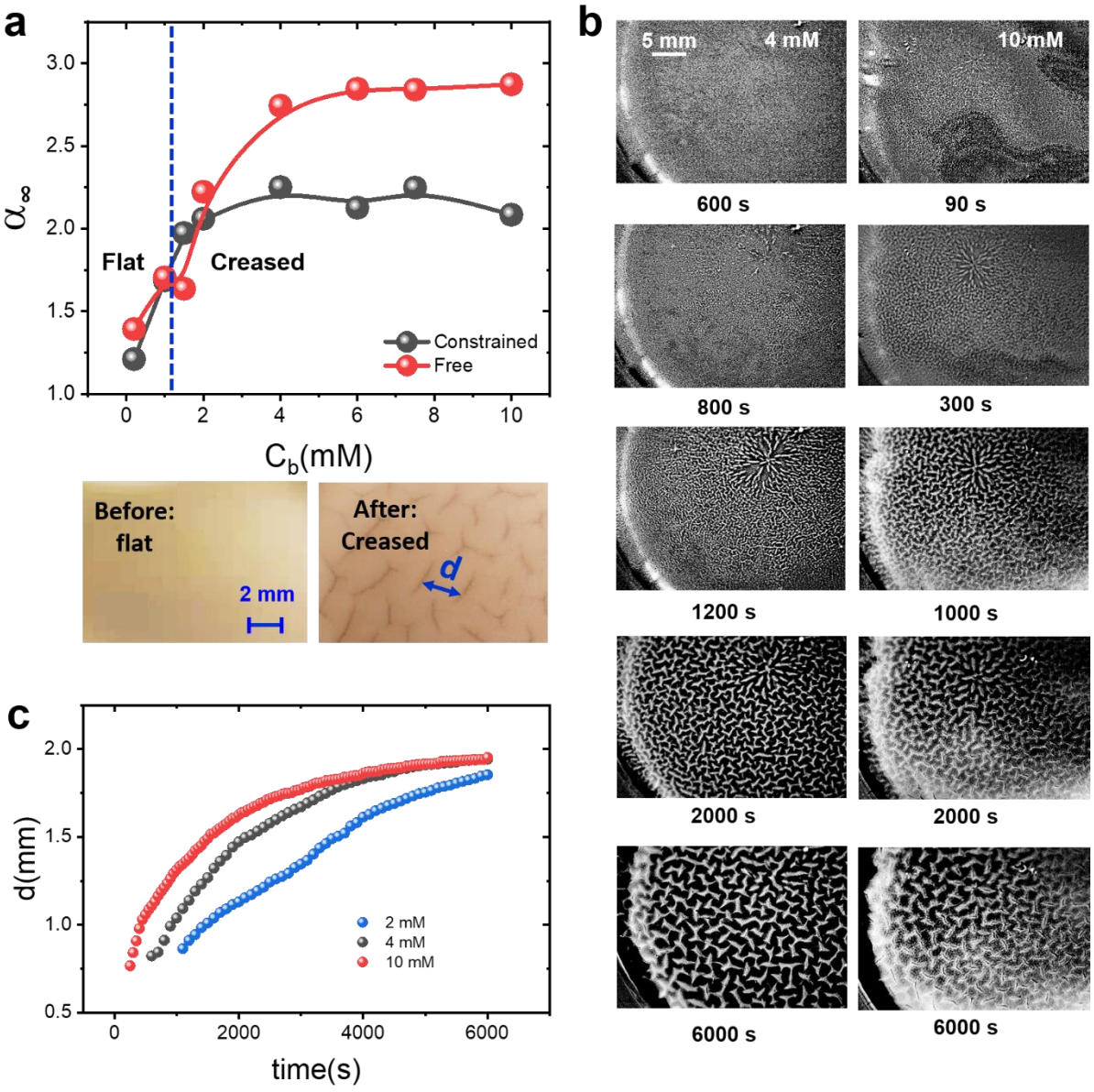

Fig. 2 *(a) Graph: equilibrium swelling ratio α_∞ in constrained and free swelling conditions, respectively. Creasing occurs for $C_b \geq$1.5 mM. Pictures: magnified view of the sample with $C_b = 6$ mM, before and after 2 days of swelling, respectively. (b) Images of gel surface taken at different swelling times (left row: C_b = 4 mM; right row: C_b = 10 mM). (c) Crease wavelength d for different C_b as a function of time.*

After being exposed to the borax solutions, the topmost part of the gel immediately reaches equilibrium, such that the local swelling ratio in a thin layer at the gel surface is equal to the maximal swelling ratio α_∞ [19, 24]. Following the equilibrium analysis, with high C_b (over 1.5 mM) where creasing can be eventually induced, creasing should be observable immediately after immersing in the solvent, as $\alpha_\infty > \alpha_c$ is reached in the topmost thin layer [11, 17]. However, creasing is in fact observed only after an induction period of 100 to 1000 s, depending on C_b. The existence of this C_b-dependent

induction period shows that the transient critical swelling ratio differs from α_c from the equilibrium measurement [5].

III. MSDWS unveils multi-scale dynamics

The results shown in Fig. 2 confirm that our experiments can characterize morphologically the nucleation and growth of creases during the swelling of a PVA chemical gel, finding features consistent with previous works [5, 17, 18]. Next, we show that high-resolution MSDWS allows also for the spatial mapping of microscopic fast events, where the transient dynamic behavior at short time scales is highly heterogeneous and deviates from existing models for swelling and creasing.

In MSDWS measurements, the sample is illuminated by an expanded laser beam and the temporal fluctuations of the intensity of the light backscattered by a small amount of probe particles dispersed in the gel provides information of the network dynamics. By fitting the ensemble-averaged autocorrelation function (described in **APPENDIX B**), we obtain the characteristic time $\tau_0(t)$ of the decay of the scattered intensity autocorrelation function. Remarkably, the change in surface topography is not observable in MSDWS measurement, as the fluctuation of speckle intensity under laser illumination due to deformation field from swelling is dominating with the short exposure time (3 ms). The characteristic decorrelation rate ν_0=1/τ_0 is used here to quantify the time scale of the dynamics and a larger value of ν_0 corresponds to faster dynamics. Using classical macroscopic analysis methods where swelling is assumed to be governed by cooperative diffusion, the corresponding value of ν_0 due to the affine deformation of the gel can be estimated to be in the range 0.01 to 10 s^{-1} in the experimental conditions used here (see **APPENDIX B** for details). In the following, we analyze the gel dynamics, gauging our experimental results with respect to these time scales.

A. Fast dynamics beyond swelling kinetics

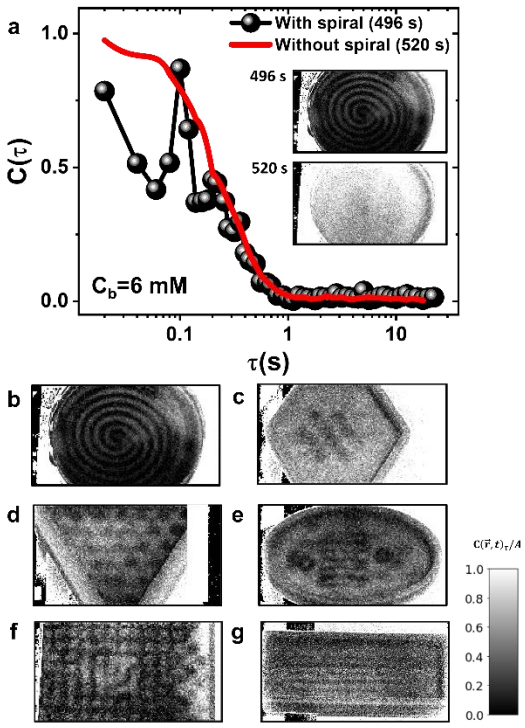

Fig. 3 *(a) Autocorrelation functions averaged over the whole surface, taken at 496 s (with spiral) and 520 s (without spiral), respectively. Inserted images: corresponding DAM for both curves at time scale of 20 ms ($C(\vec{r})_{20\,ms}$). (b~g) DAMs for containers with different geometries: round (b), hexagonal (e), equilateral triangle (d), ellipsoidal (e), square (f) and rectangular (g) The gel thickness is about 2 mm for all the containers. Normalized correlation values are coded in grey levels, as indicated by the scale bar (In the rest of DAMs in this paper, we use the same scale bar without indicating it repeatedly).*

The time scale of the global dynamics is described by ν_0 averaged over the whole gel surface. From these global dynamics measurements, the fitted ν_0 values range from 0.01 to 2 s^{-1}, corresponding to dynamics dominated by the affine deformation associated with swelling. However, at time scales much faster than that of swelling, a different dynamics response is observed. Dynamic activity maps (DAMs) are calculated to visualize the spatial distribution of the dynamics ***(APPENDIX B)*** [34] on a given time scale, and a darker color indicates faster dynamics. In the DAM ($C(\vec{r},t)_{20\,ms}$) quantifying the dynamics on the time scale of 20 ms, a spiral-shaped pattern is

randomly and intermittingly observed, causing a drop in the correlation value averaged over the whole surface (**Fig. 3**(a)). Once the spiral disappears, the decorrelation recovers a value consistent with that seen when no spirals are present. This transient spiral pattern can be observed either before or after the macroscopic observation of creasing, starting from the time the gel is immersed in the swelling fluid. In **Fig. 3(a)**, a local full decorrelation can be observed at time interval τ = 20 ms (black region in the DAMs) indicating that $\nu_0 \gg 50\ s^{-1}$, which cannot be attributed to the affine deformation associated with swelling. The change in the fast dynamics distribution is visualized by a high-speed camera with a frame frequency of 6000 frame/s for the case of swelling in the round container and results are shown in Fig. S1. We discovered that the high dynamics region in the spiral was rotating with a speed of around 25 cycle/s without radial propagation. The pattern motion and change in intensity can be observed clearly in movie S1. Interestingly, when the same constrained swelling experiments are performed in containers with different geometries, a clear dependence of the fast transient pattern on the boundary condition is observed. For hexagon and triangle containers (**Fig. 3(c)** and **(d)**), isolated spots are generated with a distance of about 10 mm from each other. For an elliptical container (**Fig. 3(e)**), the pattern loses its symmetry compared to the round container in (**Fig. 3(b)**)) and shows multiple highly active regions. Comparing square (**Fig. 3(f)**) and rectangular (**Fig. 3(g)**) containers, it can be observed that streaks of intense dynamical activity are only observed parallel to the direction of the longest side of the rectangular container.

The reversibility and geometry dependence of the patterns strongly suggests an elastic instability. In the constrained swelling geometry, compression and energy release may produce a self-oscillation state, which is similar to what was observed in Faraday experiments where capillary spiral waves can be induced by an oscillating gravity field [38]. The appearance of these patterns before creasing clearly indicates that significant compressive stresses are generated even before macroscopic creasing occurs. The observed dynamics are the result of the overlapping between the fast heterogeneous dynamics and the dynamics due to swelling occurring at longer time scales. Transient decorrelation is much faster than the time scale of the decorrelation due to swelling and only observable in a small part of our collected data: it contributes strong high-frequency fluctuations but does not influence the fitting of ν_0 and the visualization of the dynamics at longer time scales.

B. Spatially and temporally heterogeneous swelling kinetics

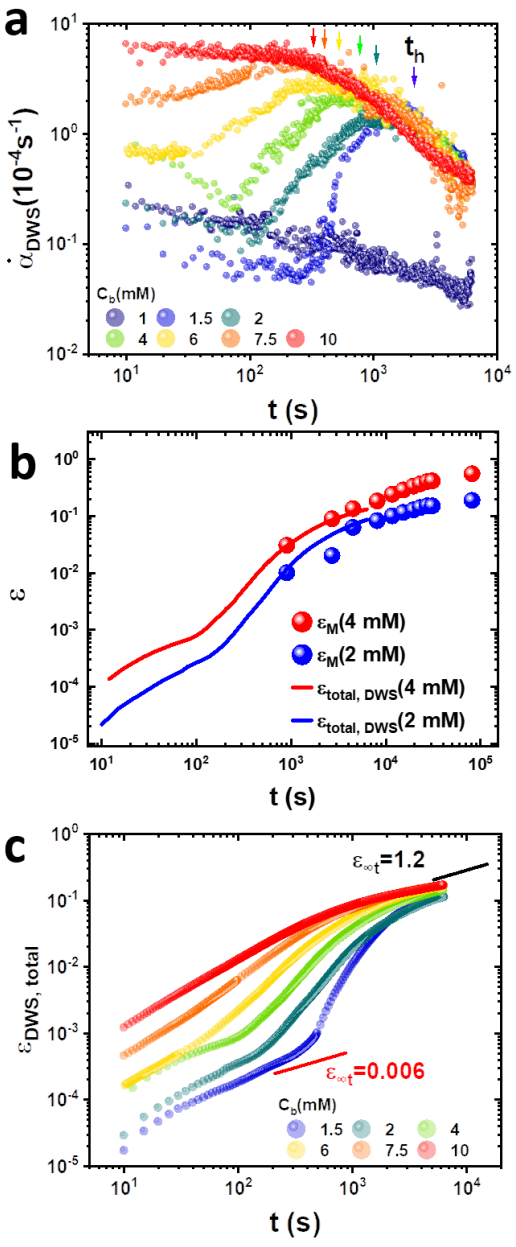

Fig. 4 *(a) Global swelling rate $\dot{\alpha}_{DWS}$ as a function of time measured during swelling in solutions with different values of C_b. The onset time of homogeneous creasing t_h are indicated by arrows. (b) Growth of the*

swelling ratio, $\varepsilon = \alpha - 1$, of the whole gel measured by mass (ε_M) and calculated from DWS ($\varepsilon_{total,DWS}$), at C_b = 2 and 4 mM. (c) $\varepsilon_{DWS,total}$ as a function of time for creased gels. Fitted value $\varepsilon_{\infty t}$ at the initial and creased states are indicated.

In addition to the mass measurements of the swelling ratio (**Fig. 2(a)**), temporally and spatially resolved swelling kinetics can be obtained from the analysis of MSDWS data, with much better temporal resolution and no need of removing the sample form its container to weight it. Based on previous work [5, 19, 24, 39], after macroscopic creasing occurs, the gel may be assumed to reach a quasi-static state and the average swelling ratio may be described by classical 1D swelling models based on the diffusion equation. Using for convenience the incremental swelling ratio $\varepsilon = \alpha - 1$ as the variable quantifying swelling, at short time scale, one finds

$$\varepsilon = \frac{2\sqrt{D_{co}t}}{h\sqrt{\pi}}\varepsilon_\infty \qquad (1)$$

D_{co} is the cooperative diffusion coefficient, around 2.2×10^{-7} cm^2/s in the studied condition [40], and t is the time after the onset of swelling. h is the initial thickness of a gel layer. For the mass measurements (ε_M), h is equal to the initial gel thickness H_0 = 1.85 mm during measurements of the whole gel; For MSDWS experiments (ε_{DWS}), h is equal to the detection length L from which most of the detected photons are issued. L is of the order of a few l^* and needs to be experimentally determined, as discussed in the following.

The global swelling rate $\dot{\alpha}_{DWS}$ for different C_b is directly calculated from MSDWS (as explained in **APPENDIX B**) and shown in **Fig. 4(a)**, as a function of t. For C_b < 1.5 mM, $\dot{\alpha}_{DWS}$ has a very low value around 10^{-5} s^{-1} and slowly decreases with time. In this regime, no significant C_b dependence was observed. At C_b = 1.5 mM where creasing is induced, we found a different behavior. $\dot{\alpha}_{DWS}$ increases with t after an initial plateau around 500 s, and starts to drop again for t > 2000 s. The same non-monotonic behavior was observed for all the higher values of C_b, and the rate of increase $\ddot{\alpha}$ before the drop decreased with C_b.

To gain insight on the non-monotonic behavior of $\dot{\alpha}_{DWS}$, we inspect the surface morphology at various times. To this end, images are averaged over a time interval longer than the decorrelation time of the speckle intensity (**APPENDIX B**), but short in comparison to the surface evolution. This allows the surface morphology to be clearly observed, by averaging out the speckled appearance of the images. Interestingly, we find that for all C_b above 1.5 mM, around the time range where $\dot{\alpha}_{DWS}$ peaks and subsequently decreases, creasing becomes homogeneously distributed. The transition time t_h deduced from the evolution of $\dot{\alpha}_{DWS}$, corresponds indeed to the time scale of homogenization and ranges from about 300 s (C_b =10 mM) to 2000 s (C_b=1.5 mM), as indicated by the arrows in **Fig. 4 (a)**. The scale of t_h is confirmed by the comparison with better visualization as in **Fig. 2(b)**. With MSDWS, the swelling ratio can be obtained by the time integration of $\dot{\alpha}_{DWS}$:

$$\varepsilon_{DWS}(\vec{\boldsymbol{r}}, t) = \int_0^t \dot{\alpha}_{DWS}(\vec{\boldsymbol{r}}, T)dT \qquad (2)$$

By imposing that the swelling of the whole gel calculated from MSDWS ($\varepsilon_{total,DWS}$) superimposes to the ε_M, by setting $\varepsilon_{total,DWS} = \frac{L}{H_0}\varepsilon_{DWS} = \varepsilon_M$ (see Eq. (1)) with L as an adjustable parameter, we found an excellent agreement between ε_M and $\varepsilon_{total,DWS}$ with $L \approx 0.4$ mm (**Fig. 4 (b)**). This confirms that MSDWS measurements allow us to precisely quantify swelling. Importantly, MSDWS has an obvious advantage over macroscopic mass measurements, in that it allows to determine the spatially resolved swelling evolution without perturbing the sample. At the longest time scale around 10^5 s, swelling still follows $\varepsilon \sim \sqrt{t}$, showing that swelling is in the early stage, well before equilibrium [18].

When the global swelling ratios $\varepsilon_{DWS,total}$ for all C_b are plotted in a double logarithmic scale (**Fig. 4 (c)**), it is clear that the swelling kinetics cannot be simply described by a 1D diffusion model. For a fixed geometry and system, Eq. (1) shows that ε(t) depends only on time and the equilibrium swelling ε_∞ ($\varepsilon_\infty = \alpha_\infty - 1$), which is a function of C_b , corresponding to the final state of the swelling. As fitted ε_∞ from swelling kinetics is not constant at the different stage of swelling and ε_∞ essentially indicates the scale of the swelling kinetics, here we applied the transient fitted value $\varepsilon_{\infty t}$ as a characteristic rate of swelling. The initial growth of $\varepsilon_{DWS,total}$ approximately follows $\varepsilon_{DWS,total} \propto t^{0.5}$ for all C_b, the scaling predicted by diffusion equation. However, when we try to describe the swelling kinetics with the diffusion equation, the $\varepsilon_{\infty t}$ value obtained by fitting Eq. (1) to these early stages is found to range from about 0.006 (1.5 mM) to 0.05

(7.5 mM), much smaller than the actual equilibrium value ($\varepsilon_\infty \approx 1.2$) reached after creasing (Fig. 2(a)). For C_b<1.5 mM, the swelling rate follows the same time dependence until the end of the measurement period. For higher C_b where creasing is observed, ε_{DWS} accelerates with respect to its initial behavior ($\varepsilon_{DWS,total} \propto t^\beta, \beta > 0.5$), corresponding to the increase in $\dot{\alpha}_{DWS}$ observed in **Fig. 4 (a)**. During the homogeneous creasing state (after t_h), the swelling ratios approach the same asymptote again, where $\varepsilon_{DWS,total}$ is proportional to $t^{0.5}$. In this final regime, the fitted values of $\varepsilon_{\infty t}$ are close to the equilibrium value ε_∞ = 1.2 for all C_b. From these observations, it can be inferred that initially swelling is highly reduced due to compression, as signaled by a value of $\varepsilon_{\infty t}$ smaller than that eventually observed in the creased state (ε_∞), which is at equilibrium. The deviation from the diffusion model before creasing indicates that the swelling kinetics is also coupled to the creasing transition. From the comparison of free and constrained swelling (**Fig. 2(a)** and previously reported results [20, 32]), it is seen that ε_∞ depends strongly on the confinement condition. It is reasonable to believe that $\varepsilon_{\infty t}$ increases after creasing, because the compressive stresses can be released by the creasing motion. However, the increase of $\varepsilon_{\infty t}$ shows a self-acceleration of the swelling kinetics and a spontaneous breaking of a metastable equilibrium is expected during the transition period (ranging from 150 to 1000 s depending on C_b), the sign of which should be detectable by MSDWS.

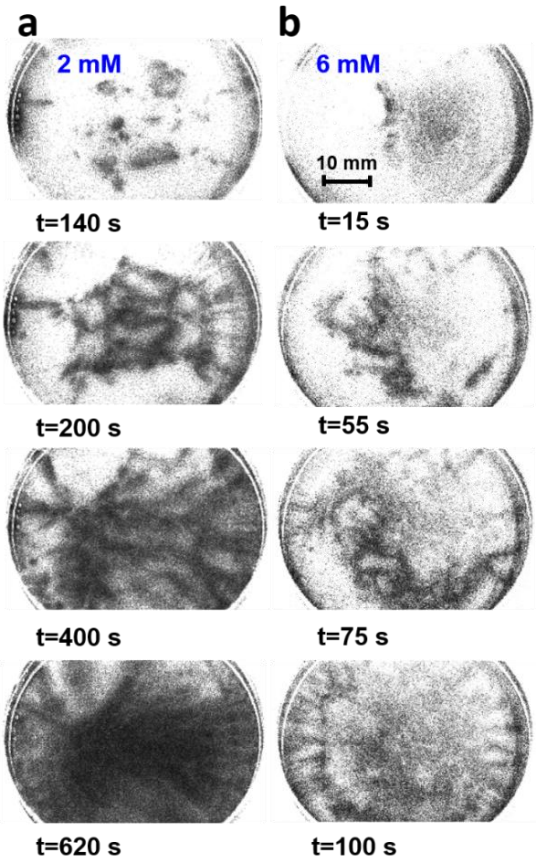

Fig. 5 *Time-averaged DAMs before creasing, with τ = 0.1 s at (a) C_b = 2 and (b) 6 mM.*

Time-averaged DAMs $\overline{C(\vec{r},t)_\tau}$ (see **APPENDIX B)** are calculated to characterize the spatial heterogeneity of swelling, where only the differences in the dynamics occurring over the time scale of the relaxation of correlation functions due to affine deformation are shown. As seen in the $\overline{C(\vec{r},t)_{0.1\,s}}$ maps of **Fig. 5**, initial dynamics are homogeneous over the whole sample. During the time interval where the global $\dot{\alpha}_{DWS}$ increases (before 1100 s for C_b =2 mM and before 500 s for C_b =6 mM, see **Figs 5(a)** and **5(b)**, respectively), there are some signs of nucleation of regions with swelling rates faster than the global $\dot{\alpha}_{DWS}$. The onset of the heterogeneous swelling results in the accelerated swelling seen in the spatially-averaged data of **Fig. 4(c)** in the intermediate period.

To better relate local dynamics (swelling rate) and creasing morphology at the onset of the creases nucleation, a separate measurement was performed, with a smaller field of view and a better spatial resolution (20 µ m/pixel), by switching image acquisition between white light illumination (for

crease visualization) and laser illumination (for dynamics measurement), for C_b = 6 mM. In **Fig. 6(a)**, at *t*=360 s, the heterogeneous nucleation of creases can be observed, while growth pattern of the creases matches with pattern of $\overline{C(\vec{r},t)_{1\,s}}$ in **Fig. 6(b)**. The dynamic activation of the nucleation spot can be seen in the DAMs (*t* = 240 s and 340 s) and conventional images (*t* = 360 s and 600 s). Since nucleation of creases is expected to be sensitive to structural defaults in the gel, this result suggests that MSDWS can be used to detect defects and predict heterogeneity in mechanical instabilities. The growth of a region with fast dynamics can be observed, similar to **Fig. 5**. It can be noticed in **Fig. 6(c)** that the diffusive patterns are actually formed by the scattered spots (diameter around 0.2 mm) and their surrounding regions, with faster swelling rates. This indicates that the region with faster dynamics in **Fig. 5** corresponds to the onset of creases with a small, submillimetric initial size. The folding motion during creasing results in a local fluctuation of the swelling rate, in the form of spot patterns detected in the $\overline{C(\vec{r},t)_{\tau}}$ maps.

Based on the results of **Fig. 5** and **6**, we discover that the unusual jump of the extrapolated final state (fitted $\varepsilon_{\infty t}$ from below 0.05 to 1.2 in **Fig. 4(c)**) is achieved via an intermediate heterogeneous creasing and swelling stage. In this transition period, the overall swelling rate is even faster than that close to the equilibrium state after creasing. This can be caused by two effects: (a) the process of breaking the confinement and releasing the accumulated elastic energy in the compressed flat state can contribute to this faster swelling rate [1, 29]; (b) heterogeneous swelling indicates a locally less-constrained swelling mode, whose final ε_{∞} can be much larger than that in the constrained state.

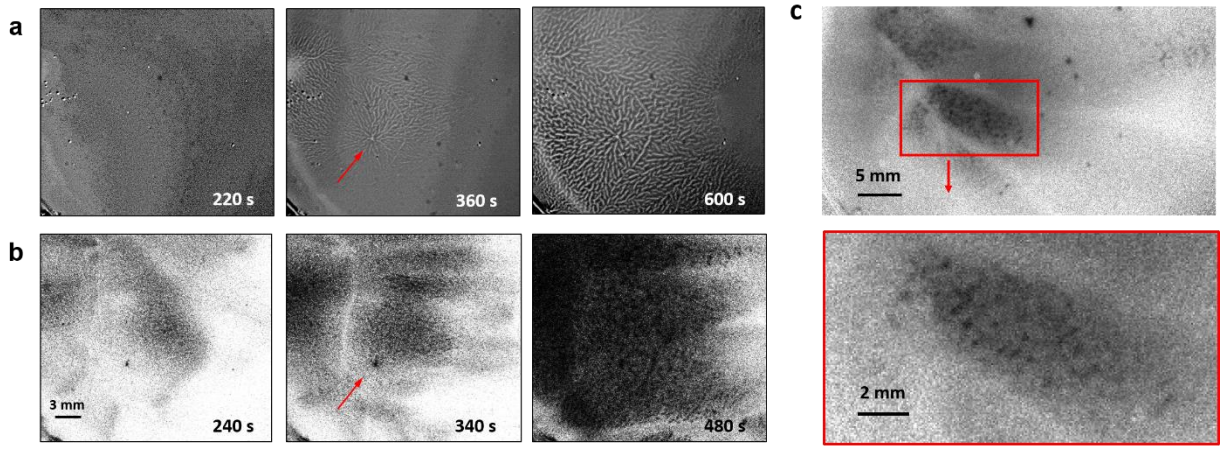

Fig. 6 *(a) Crease images (with white light illumination) at different time after swelling. (b) Time-averaged DAM* $\overline{C(\vec{r},t)_{1\,s}}$ *for* C_b*=6 mM, quantifying the dynamics in the same region as in (a). (c) DAM map during a separate experiment for* C_b*=6 mM with longer exposure time (50 ms) and better image quality.*

Creasing during swelling brings another question: the increase of the wavelength of the pattern during further swelling after the onset of creasing. The growth of the pattern, i.e., the increase of the inter-crease spacing *d* (**Fig. 2(c)**), takes place in a confined geometry with a constant size, so that the overall number of creases is decreasing. This cannot be simply described as a self-similar growth [18], but rather as a process involving a continuous adjustment of the crease distribution. Taking advantage of spatially resolved MSDWS, the local deformation related to creasing during the growth of the creases can also be visualized.

During homogeneous creasing, a heterogeneous distribution of spot-like patterns of high dynamics regions are observed through time-averaged DAMs, as shown in **Fig. 7(a)** (C_b = 6 mM and τ = 0.1 s). With time after t_h, the average dynamics decelerate as seen in **Fig. 4(a)** (the DAMs becoming brighter), while the distance between the spots increases. Interestingly, each spot exhibits a flickering (with periodicity of about 100 s), indicative of intermittent activity, as shown for one representative high dynamics spot in the series of zoomed images of **Fig. 7(b)**. Dynamics peaks at *t* = 1800 s, as seen from both the DAMs and the temporal

evolution of the fitted value ν_0 of the relaxation rate of the intensity autocorrelation function. The active phase of each spot occurs at different times and the whole DAM exhibits flickering high dynamics spots at different locations (**movie S2**, 25 ×).

In order to understand the relationship between these local activation events and the surface morphology, we integrate the DAMs over a period longer than the lifetime of the active spots and compare the DAMs of the cumulated dynamics to the surface images of the same region in **Fig. 7(c)**. The comparison shows that the high dynamics spots and the creases are spatially related and that the high dynamics spots correspond to the gap between the creases. The wavelength of the cumulated dynamics spots d_{spot} has the same value as d, as confirmed by 2D-FFT processing (**Fig. 9** in **APPENDIX B**). The increase of d_{spot} can be visualized in the cumulated DAMs at different times (**Fig. 7(a)**). Thus, we infer that the high dynamics spots are due to the rearrangement of creases. This further confirms the results of Fig. 6, and the folding and rearrangement of creases both lead to local fluctuation of the swelling rate. More importantly, the fluctuations of the high activity spot pattern, correspond to local adjustments of the crease distribution, thus indicating that the growing creases are still spatially heterogeneous, even when their distribution is already homogeneous.

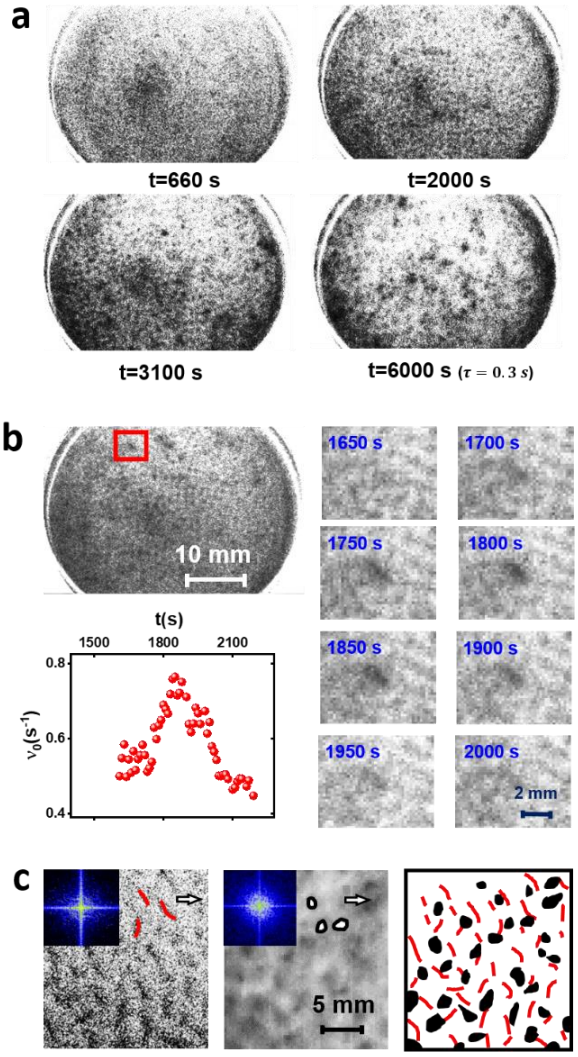

Fig. 7 *(a) DAMs of cumulated dynamics at different times for C_b = 6 mM and τ = 0.1 s. (b) Spot patterns and local changes of one spot (C_b = 6 mM, τ = 0.1 s) in DAMs around t = 1800 s. (c) Surface image (left panel) and corresponding cumulated DAM (middle panel) at t = 5600 s. 2D-FFT spectra are inserted in the images. The locations of the creases and spot patterns are indicated schematically in the right panel.*

IV. Summary

This work applies MSDWS to the measurements of spatio-temporal transitions in the dynamics of a complex system, where we almost push the application to its limit, with time resolution around 0.1 ms and spatial resolution around 100 μm. Due to the lack of characterization methods, such transient behavior has

not been reported so far and points to the existence of metastable states. We discovered that the initial behavior is rather complex and deviates from existing models considering only 1D diffusion kinetics. In addition to the well-known result that creasing nucleation and growth is governed by the swelling, [5, 17] we discovered that the swelling kinetics is conversely influenced by the creasing transition. The interaction between compression and surface instability results in an unusual heterogeneous swelling and creasing (**Figs 5** and **6**), even though the gel is initially homogeneous in the plane. In fact, considering limited diffusion kinetics, the effect of heterogeneous swelling should commonly exist in transient swelling phenomena, and here we experimentally demonstrated it for the first time. Our work shows a convenient tool to visualize and quantify the transient behaviors in poroelastic materials. Even after creasing becomes visible and the global swelling kinetics coincides with equilibrium models governed by the 1D diffusion equation, the rearrangement events during the growth of the crease structure result in spatially and temporally heterogeneous swelling events between the creases, not accounted for by the 1D diffusion equation. In the practical application of surface patterns generated in a similar condition, the time scale for the delayed nucleation and post-stabilization of the pattern can be evaluated with the tool demonstrated in this work.

In summary, in-situ measurements of surface creasing during swelling provides information on the transient stages toward equilibration and unveils rich heterogeneous behaviors in well-controlled conditions. With these high temporal resolution methods, transient behaviors and the existence of metastable states can be experimentally characterized and our results unveil how such large instabilities, which in principle may have large activation energies, can occur kinetically by a sum of smaller steps with a much lower activation barrier. Such a stepwise process in the onset of instabilities may be more widespread than gel swelling and the knowledge of the intermediate steps may lead to more realistic modeling and predictions of the kinetics of the transition and help the design of a new generation of knowledge-based responsive materials.

Acknowledgements

This work is financially supported by European Union's Horizon 2020 Programme for Research and Innovation under the Marie Skłodowska-Curie grant agreement no. 765811 (DoDyNet). This work is partly supported by ANR (project GELWET, ANR-17-CE30-0016 and project MultiNet, ANR-20-CE06-0028,). L.C. acknowledges support from the Institut Universitaire de France.

J.J. and T.N. designed and performed the experiments. J.J, T.N., L.C. and C.C. designed and built the measurement set-up. K.S., T.N., L.C. and C.C. participated to the processing and interpretation of the data. J.J. wrote the manuscript with contributions from all the authors. All authors have approved the final version of the paper.

Data Availability

ASCII and tif. format images for all the datasets shown in the figures of the main text and SI Appendix are deposited in Zenodo (DOI: 10.5281/zenodo.5915016).

APPENDIX A: Gel preparation and swelling

We use a well-known system comprising poly(vinyl alcohol) (PVA) and borate ions (generated by dissolution of sodium tetraborate, borax), and different borax concentrations (C_b) are applied to tune the swelling kinetics and to induce a large increase in the equilibrium swelling ratio [41, 42]. PVA with weight-averaged molecular weight of 89 000–98 000 g/mol and glutaraldehyde (GA) as a cross-linker were purchased from Aldrich. PVA powder was dissolved in deionized water at 90 ℃ and stirred over 10 hours at a concentration of 8.8 wt%, as a stock solution. Chemically cross-linked PVA hydrogel was prepared in an aqueous mixture with PVA (4.4 %), GA (5 mM), and hydrochloric acid (HCl, 0.05 mM). Prior to the gelation, polystyrene nanoparticles (from Micromod, diameter: 500 nm, concentration: 1 %) were added as probes for MSDWS measurements.

The preparation and measurement process are shown in **Fig. 1(b)**. 4 ml of solution before chemical cross-linking was poured into a round plastic petri dish with a radius of 55 mm, giving a solution thickness of 1.68 mm. The solution was then sealed for 10 h for the PVA chemical cross-linking to occur. The chemical gel was then washed in pure water for 24 h to remove HCl. HCl acts as a catalyst for chemical cross-linking but cannot coexist with $\mathrm{B(OH)_4}^-$[43]. During the washing step, the PVA gel slightly swells (to α = 1.1 and H_0 = 1.85 mm), during which no surface morphology change was observed. In order to further swell the gel and induce the surface morphology change, the gel was immersed in a solution of borax (sodium tetraborate, from Aldrich) with different concentrations (0.2 ~ 10 mM). Borate ions diffuse into the gel and make a didiol complex with the hydroxyl groups on the PVA chains. The same

molarity of sodium ions as counterions also diffuses into the gel for electroneutrality, inducing the gel swelling due to the osmotic pressure.

APPENDIX B: Data collection and processing

1. Image collection

MSDWS was performed during the complexation and swelling of the chemical gel. The whole gel surface was illuminated homogenously with a divergent laser beam (Excelsior-532-300-CDRH, 300 mW, wavelength 532 nm), as shown in **Fig. 1(b)**. Speckle images were collected by a CMOS camera (BASLER acA2000-340km) equipped with a polarizer. The polarizer axis was oriented so as to reject the singly scattered light. Time resolution was set in different scales from 5 to 300 ms and the pixel size corresponded to 32 µm/pixel in the sample, with image size of 2048x1088 pixels. The exposure time of a raw image was 3 ms to optimize the time resolution and speckle appearance. For the observation of the fast dynamics at the scale of around 0.1 ms, a fast camera (Photron FASTCAM SA3) was used with a frame rate of 6000 frames per second and a pixel size of 125 µm/pixel in the sample, with image size of 512 × 512 pixels.

2. Processing of raw speckle images

Examples of raw speckle images are shown in **Fig. 8** (a), the first one of which is collected at 3000 s for a borax concentration (C_b) of 6 mM. Even though creases have already been generated, the morphology feature is barely observable in the speckle images. The intensity difference due to a height difference due to surface features is hidden by the spatially fluctuating intensity of speckles generated by the laser illumination. It has been checked that up to 2 h the creases do not contribute to the autocorrelation function. MSDWS characterization is still valid since the height difference due to creasing and swelling is negligible (~1 mm), compared to the distance from the camera to the sample surface (~20 cm). To detect the change in surface morphology, a series of raw images are averaged over a time interval $\Delta t(t)$ larger than the decorrelation time $\tau_0(t)$ of the speckle pattern, so that the speckles are smeared out by the averaging of uncorrelated images. The raw image right after adding the borax solution is used as a background to highlight the crease structure, as seen in **Fig. 8 (b)**. With this method, both space resolved dynamics and surface morphology can be observed simultaneously with no need of a separately imaging the gel surface with a laser and a conventional light source. However, at the early stage of creasing, the initial size and depth of the creases is too small to be measured this way, so that white illumination is still applied (**Fig. 6(a)**), and images are taken with an exposure time of 1 ms.

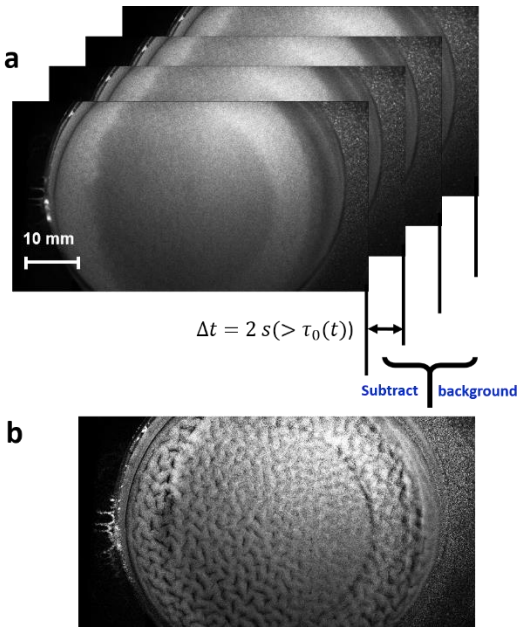

Fig. 8 *Series of raw images where surface features are hidden due to the spatial fluctuations of intensity associated to speckles. (b) Surface images obtained by averaging the raw images over a time interval* $\Delta t = 2$ s.

3. Fitting of the autocorrelation function

In the backscattering geometry, MSDWS analyzes the temporal fluctuations of the back-scattered light. To extract the spatial and temporal dynamics information during the swelling, a spatially and temporally resolved intensity autocorrelation function $C(\vec{r}, t, \tau)$ is calculated:

$$C(\vec{r}, t, \tau) = \frac{\langle I_p(t) I_p(t+\tau)\rangle_{\vec{r}}}{\langle I_p(t)\rangle_{\vec{r}} \langle I_p(t+\tau)\rangle_{\vec{r}}} - 1 \qquad (3)$$

where I_p is the intensity of the p-th pixel, and $\langle \dots \rangle_{\vec{r}}$ designates an average over pixels belonging to a small region centered around position $\vec{r}$. t is the time after swelling and τ is the time delay. At fixed t and $\vec{r}$, the autocorrelation function can be expressed in an exponential form as a function of τ [44, 45]:

$$C(\tau) = A exp\left(-2\gamma\sqrt{\left(\frac{\tau}{\tau_0}\right)^2 + a}\right) + B \quad (4)$$

γ is a coefficient depending on the polarization condition of the incident/detected light. In our experiments, a polarizer is applied to remove singly scattered light so that a value γ = 2.7 was used [46, 47]. a is determined by the ratio between the transport mean free path l^* [33] and gel thickness [44, 45]. In a fixed geometry and test condition, a should be a constant value. We found that a is around 0.015 from the measurement of a slower swelling (at low C_b), but the precise fitting strongly depends on the data quality at short time scale ($\tau \ll \tau_0$). In this work, a is set as a fixed parameter of 0.015 for all the fitting. τ_0(t) corresponds to the time over which the probe particles are displaced by a distance of the order of 50 nm (1/ k). k is the wave vector of the incident light ($k = 2\pi n/\lambda$, λ = 532 nm, *n* = 1.4 is the index of refraction) [48].

The measured dynamics probed by the decorrelation of the backscattered light can be due to a number of different mechanisms [49, 50]. The affine deformation field during swelling is expected to result in microscopic ballistic motion [47, 51] while the disturbance due to compression and local heterogeneity may lead to an additional non-affine contribution to the displacement of the particles [49, 50, 52, 53]. In the case where the time scales of different contributions overlap with each other, the analysis becomes rather complex [49, 50]. Fortunately, although the time scale of additional non-affine contributions is unknown, the relationship between the time scale of the ballistic dynamics and the affine deformation rate is well studied [47, 50]. For a purely affine deformation with no additional dynamics, the autocorrelation function can be related to the strain field [44, 45] by:

$$C(\tau) = Aexp\left(-2\gamma\sqrt{3k^2l^{*2}f[U(\tau)] + a}\right) + B \quad (5)$$

where $f[U(\tau)]$ is a function of the deformation tensor U : $f[U] = [Tr^2(U) + 2Tr(U^2)]/15$. For 1D swelling under lateral confinement one has:

$$U(\tau) = \begin{bmatrix} 0 & 0 & 0 \\ 0 & 0 & 0 \\ 0 & 0 & \dot{\alpha}_{DWS}\tau \end{bmatrix} \quad (6)$$

with $\dot{\alpha}_{DWS}$ is the swelling rate ($\frac{\partial\alpha}{\partial t}$) measured by MSDWS. Hence, $f[U] = (\dot{\alpha}_{DWS}\tau)^2/5$ [47]; inserting $\tau = \tau_0 = 1/\nu_0$ in the above equations, the relationship between $\dot{\alpha}_{DWS}$ and ν_0 is found to be:

$$\dot{\alpha}_{DWS}(t) = \sqrt{\frac{5}{3}}\frac{\nu_0}{kl^*(t)} \quad (7)$$

The corresponding scale of ν_0 associated with swelling can then be estimated from the theoretical swelling kinetics estimated using the diffusion equation, Eq. (1), using α_∞ as obtained from mass measurements (**Fig. 2(a)**). The swelling rate $\dot{\alpha}$ is proportional to ν_0/l^*, where l^* has initial value l_0^* around 0.2 mm at the studied condition [40]. During swelling, l^* increases because the volume fraction of the tracer particles decreases. For 1D swelling, the volume fraction is inversely proportional to α, such that $l^*(t) \approx \alpha l_0^*$. MSDWS provides the averaged dynamics in a "detection thickness" L, corresponding to the topmost layer of the gel from which most of the detected photons are issued. The thickness of this layer corresponds to a few l^* [54] and can be estimated by matching the swelling measured by DWS with that obtained from mass measurements, as described in **Sec. III. B**. Here, we simply set $L = 1$ mm to estimate the expected range of ν_0 values, in order to distinguish between the time scales of the different contributions to the observed dynamics. In the time scale of the experiments (10000 s), the cooperative diffusion length ($\sqrt{2D_{co}t}$, cooperative diffusion coefficient D_{co} around 2.2×10^{-7} cm^2/s [40]) is smaller than L, so that the increase of the swelling ratio (α-1) is protional to $t^{0.5}$ [19, 24]:

$$\frac{\alpha-1}{\alpha_\infty-1} = \frac{2\sqrt{D_{co}t}}{L\sqrt{\pi}} \quad (8)$$

One thus has:

$$\dot{\alpha} = \frac{(\alpha_\infty-1)\sqrt{D_{co}}}{L\sqrt{\pi t}} \quad (9)$$

In the experimental time scale from 100 s (after the initial spreading and wetting on the surface) to 10000 s, $\dot{\alpha}$ varies from 3×10^{-4} s^{-1} to 3×10^{-5} s^{-1}. The order of magnitude of ν_0 can thus be applied as an indicator to distinguish different contributions to dynamics. Considering the change of α from 1 to 2.2, the relaxation rate ν_0 due to the contribution of the affine deformation is found to range approximately from 0.01 to 10 s^{-1}.

4. Time-averaged dynamic activity maps

For the visualization of the spatial heterogeneity of the dynamics during swelling, spatially-resolved correlation functions $C(\vec{r}, t)_\tau$ were calculated as a function of position $\vec{r}$ and time *t*, using a fixed time interval τ. Here, $\vec{r}$ is the center of a region of interest (ROI) with size 6x6

pixels. $\mathrm{C}(\vec{\boldsymbol{r}},t)_\tau$ is converted to a grey scale intensity and shown as a dynamic activity map (DAM) [34, 36, 51]. The faster the local dynamics, the lower the correlation function at a fixed τ. Hence, darker shades in the DAMs correspond to regions with faster dynamics.

To separate the fast dynamics from the characterization of longer time scales, time-averaging is applied using the following equations:

$$\overline{C(\vec{\boldsymbol{r}},t,\tau)} = \frac{\langle \bar{I}_t \bar{I}_{t+\tau} \rangle_{\vec{r}}}{\langle \bar{I}_t \rangle_{\vec{r}} \langle \bar{I}_{t+\tau} \rangle_{\vec{r}}} - 1 \qquad (10)$$

where:

$$\bar{I}_t = \sum_{n=-N}^{n=N} I_{t+nT} \ (T > 2\tau) \qquad (11)$$

The time-averaged autocorrelation function $\overline{\mathrm{C}(\vec{\boldsymbol{r}},t)_\tau}$ is calculated with time averaged intensity with interval *T* longer than the fast dynamics time scale (τ_0 < 20 ms). The ensemble averaging correlation is made between time-averaged intensity instead of ensemble time- and space- averaging, which would be too costly computationally. Here τ, *T* and *N* are chosen to be 0.1 s, 0.4 s and 25, for **Figs. 5** and **7**, and 1 s, 4 s, and 10 for **Fig. 6**, respectively.

5. 2D Fourier Transform processing of the images

The characteristic length of the image features (spots in accumulated DAMs and creases in surface images) can be obtained by Two-Dimensional Discrete Fourier Transform (2D-DFT) [55]:

$$F(u,v) = \sum_0^{M-1} \sum_0^{N-1} I\,(x,y) e^{-j2\pi\left(\frac{ux}{M}+\frac{uy}{N}\right)} \qquad (12)$$

$I(x,y)$ is the corresponding intensity value for each pixel in the time-averaged DAMs and surface images. The fast algorithm for computing 2D-DFT, Two-Dimensional Fast Fourier Transform (2D-FFT) is carried out with the optimized library NumPy in Python [56]. After shifting the zeroth frequency to the center, a halo can be observed in $F(u,v)$ (as seen in **Fig. 9** (a)), corresponding to the wave number of characteristic lengths (d and d_{spot}) [18, 57]. $F(u,v)$ is azimuthally integrated to obtain a one-dimensional function $F(1/D)$ in wave number space, so that the characteristic length can be quantified and compared for the conventional and DAM images, as seen in **Fig. 9(b)**. A peak was observed at the same value around 0.35 mm^{-1} for both images in 1D intensity results, which corresponds to an average distance between the crease as well as to the dynamic spot, $d_{spot} \approx d = 2.8$ mm. By checking d and d_{spot} values at different times, it has been confirmed that they have a similar value so that the characteristic length scale of the creases and that of the high dynamics spots are spatially related.

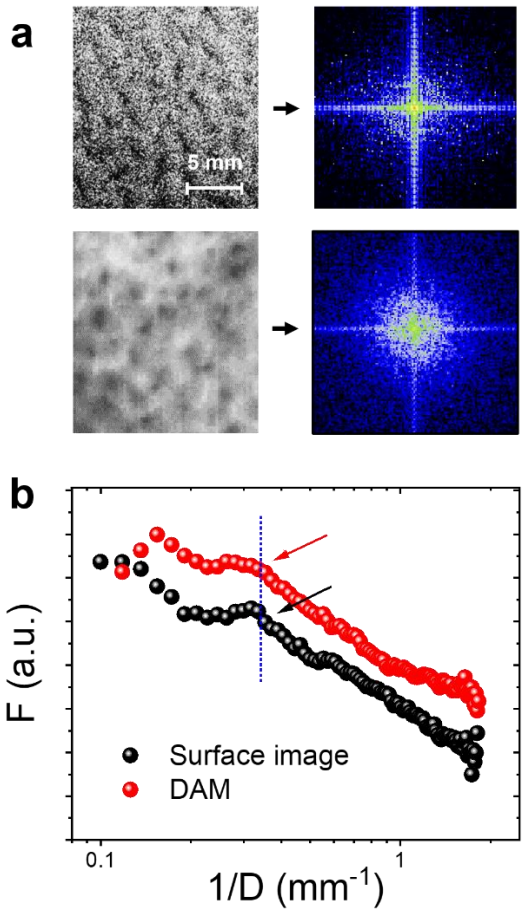

Fig. 9 *(a): Images (surface images and accumulated DAM) and corresponding 2D-FFT spectra, for t = 5600. (b) Azimuthally averaged Fourier transform* $F(1/D)$ *obtained from the 2D spectra shown in (a).*

Reference

[1] Q. Liu, T. Ouchi, L. Jin, R. Hayward, and Z. Suo, Elastocapillary Crease, Phys. Rev. Lett. **122,** 098003 (2019).

[2] T. Tanaka, S.-T. Sun, Y. Hirokawa, S. Katayama, J. Kucera, Y. Hirose, and T. Amiya, Mechanical instability of gels at the phase transition, Nature **325,** 796 (1987).

[3] M. Arifuzzaman, Z.L. Wu, R. Takahashi, T. Kurokawa, T. Nakajima, and J.P. Gong, Geometric and Edge Effects on Swelling-Induced Ordered Structure Formation in Polyelectrolyte Hydrogels, Macromolecules **46,** 9083 (2013).

[4] Q. Wang, and X. Zhao, A three-dimensional phase diagram of growth-induced surface instabilities, Sci. Rep. **5,** 1 (2015).

[5] D. Chen, S. Cai, Z. Suo, and R.C. Hayward, Surface energy as a barrier to creasing of elastomer films: an elastic analogy to classical nucleation, Phys. Rev. Lett. **109,** 038001 (2012).

[6] W. Hong, X. Zhao, and Z. Suo, Formation of creases on the surfaces of elastomers and gels, Appl. Phys. Lett. **95,** 111901 (2009).

[7] P. Ciarletta, Matched asymptotic solution for crease nucleation in soft solids, Nat. Commun. **9,** 1 (2018).

[8] J. Kim, J. Yoon, and R.C. Hayward, Dynamic display of biomolecular patterns through an elastic creasing instability of stimuli-responsive hydrogels, Nat. Mater. **9,** 159 (2010).

[9] H.S. Kim, and A.J. Crosby, Solvent-responsive surface via wrinkling instability, Adv. Mater. **23,** 4188 (2011).

[10] S. Yang, K. Khare, and P.-C. Lin, Harnessing Surface Wrinkle Patterns in Soft Matter, Adv. Funct. Mater. **20,** 2550 (2010).

[11] J. Yoon, J. Kim, and R.C. Hayward, Nucleation, growth, and hysteresis of surface creases on swelled polymer gels, Soft Matter **6,** (2010).

[12] B. Xu, D. Chen, and R.C. Hayward, Mechanically gated electrical switches by creasing of patterned metal/elastomer bilayer films, Adv. Mater. **26,** 4381 (2014).

[13] N. Zalachas, S. Cai, Z. Suo, and Y. Lapusta, Crease in a ring of a pH-sensitive hydrogel swelling under constraint, Int. J. Solids Struct. **50,** 920 (2013).

[14] K. Wu, Y. Sun, H. Yuan, J. Zhang, G. Liu, and J. Sun, Harnessing Dynamic Wrinkling Surfaces for Smart Displays, Nano Lett. **20,** 4129 (2020).

[15] F. Li, H. Hou, J. Yin, and X. Jiang, Near-infrared light–responsive dynamic wrinkle patterns, Sci. Adv. **4,** eaar5762 (2018).

[16] M.A. Biot, Surface instability of rubber in compression, Appl. Sci. Res. A **12,** 168 (1963).

[17] V. Trujillo, J. Kim, and R.C. Hayward, Creasing instability of surface-attached hydrogels, Soft Matter **4,** (2008).

[18] H. Tanaka, H. Tomita, A. Takasu, T. Hayashi, and T. Nishi, Morphological and kinetic evolution of surface patterns in gels during the swelling process: Evidence of dynamic pattern ordering, Phys. Rev. Lett. **68,** 2794 (1992).

[19] J. Yoon, S. Cai, Z. Suo, and R.C. Hayward, Poroelastic swelling kinetics of thin hydrogel layers: comparison of theory and experiment, Soft Matter **6,** (2010).

[20] N. Bouklas, and R. Huang, Swelling kinetics of polymer gels: comparison of linear and nonlinear theories, Soft Matter **8,** 8194 (2012).

[21] M. Guvendiren, J.A. Burdick, and S. Yang, Kinetic study of swelling-induced surface pattern formation and ordering in hydrogel films with depth-wise crosslinking gradient, Soft Matter **6,** 2044 (2010).

[22] W. Toh, Z. Ding, T. Yong Ng, and Z. Liu, Wrinkling of a polymeric gel during transient swelling, J Appl. Mech. **82,** 061004-1 (2015).

[23] A. Ilseng, V. Prot, B.H. Skallerud, and B.T. Stokke, Buckling initiation in layered hydrogels during transient swelling, J. Mech. Phys. Solids **128,** 219 (2019).

[24] M. Doi, Gel dynamics, J. Phys. Soc. Jpn. **78,** 052001 (2009).

[25] T. Tanaka, and D.J. Fillmore, Kinetics of swelling of gels, J. Chem. Phys. **70,** 1214 (1979).

[26] E. Hohlfeld, and L. Mahadevan, Unfolding the sulcus, Phys. Rev. Lett. **106,** 105702 (2011).

[27] E. Hohlfeld, and L. Mahadevan, Scale and nature of sulcification patterns, Phys. Rev. Lett. **109,** 025701 (2012).

[28] J. Yang, W. Illeperuma, and Z. Suo, Inelasticity increases the critical strain for the onset of creases on hydrogels, Extreme Mech. Lett. **40,** 100966 (2020).

[29] D. Chen, L. Jin, Z. Suo, and R.C. Hayward, Controlled formation and disappearance of creases, Mater. Horiz. **1,** 207 (2014).

[30] R. Takahashi, Y. Ikura, D.R. King, T. Nonoyama, T. Nakajima, T. Kurokawa, H. Kuroda, Y. Tonegawa, and J.P. Gong, Coupled instabilities of surface crease and bulk bending during fast free swelling of hydrogels, Soft Matter **12,** 5081 (2016).

[31] M. Curatolo, P. Nardinocchi, E. Puntel, and L. Teresi, Transient instabilities in the swelling dynamics of a hydrogel sphere, J. Appl. Phys. **122,** 145109 (2017).

[32] R. Marcombe, S. Cai, W. Hong, X. Zhao, Y. Lapusta, and Z. Suo, A theory of constrained swelling of a pH-sensitive hydrogel, Soft Matter **6,** 784 (2010).
[33] D.J. Pine, D.A. Weitz, J.X. Zhu, and E. Herbolzheimer, Diffusing-wave spectroscopy: dynamic light scattering in the multiple scattering limit, J. Phys. **51,** 2101 (1990).
[34] A. Duri, D.A. Sessoms, V. Trappe, and L. Cipelletti, Resolving long-range spatial correlations in jammed colloidal systems using photon correlation imaging, Phys. Rev. Lett. **102,** 085702 (2009).
[35] S. Aime, L. Ramos, and L. Cipelletti, Microscopic dynamics and failure precursors of a gel under mechanical load, Proc. Natl. Acad. Sci. U. S. A. **115,** 3587 (2018).
[36] A. Amon, V.B. Nguyen, A. Bruand, J. Crassous, and E. Clement, Hot spots in an athermal system, Phys. Rev. Lett. **108,** 135502 (2012).
[37] M.K. Kang, and R. Huang, Swell-induced surface instability of confined hydrogel layers on substrates, J. Mech. Phys. Solids **58,** 1582 (2010).
[38] S. Kiyashko, L. Korzinov, M. Rabinovich, and L.S. Tsimring, Rotating spirals in a Faraday experiment, Phys. Rev. E **54,** 5037 (1996).
[39] A. Peters, and S. Candau, Kinetics of swelling of spherical and cylindrical gels, Macromolecules **21,** 2278 (1988).
[40] T. Narita, K. Mayumi, G. Ducouret, and P. Hébraud, Viscoelastic properties of poly (vinyl alcohol) hydrogels having permanent and transient cross-links studied by microrheology, classical rheometry, and dynamic light scattering, Macromolecules **46,** 4174 (2013).
[41] J. Zhao, K. Mayumi, C. Creton, and T. Narita, Rheological properties of tough hydrogels based on an associating polymer with permanent and transient crosslinks: Effects of crosslinking density, J. Rheol. **61,** 1371 (2017).
[42] M. Shibayama, T. Takeuchi, and S. Nomura, Swelling/shrinking and dynamic light scattering studies on chemically cross-linked poly (vinyl alcohol) gels in the presence of borate ions, Macromolecules **27,** 5350 (1994).
[43] W. Luo, S. Zhang, P. Li, R. Xu, Y. Zhang, L. Liang, C.D. Wood, Q. Lu, and B. Tan, Surfactant-free CO2-in-water emulsion-templated poly (vinyl alcohol)(PVA) hydrogels, Polymer **61,** 183 (2015).
[44] F. Cardinaux, L. Cipelletti, F. Scheffold, and P. Schurtenberger, Microrheology of giant-micelle solutions, EPL **57,** 738 (2002).
[45] D. Weitz, and D. Pine, *Dynamic light scattering: The method and some applications* (Oxford University Press, 1993), p. 652.
[46] F.C. MacKintosh, J.-X. Zhu, D. Pine, and D. Weitz, Polarization memory of multiply scattered light, Phys. Rev. B **40,** 9342 (1989).
[47] M.-Y. Nagazi, G. Brambilla, G. Meunier, P. Marguerès, J.-N. Périé, and L. Cipelletti, Space-resolved diffusing wave spectroscopy measurements of the macroscopic deformation and the microscopic dynamics in tensile strain tests, Opt. Lasers Eng. **88,** 5 (2017).
[48] W. Xia, D. Piras, M. Heijblom, W. Steenbergen, T.G. Van Leeuwen, and S. Manohar, Poly (vinyl alcohol) gels as photoacoustic breast phantoms revisited, J. Biomed. Opt. **16,** 075002 (2011).
[49] X. Wu, D. Pine, P. Chaikin, J. Huang, and D. Weitz, Diffusing-wave spectroscopy in a shear flow, J. Opt. Soc. Am. B **7,** 15 (1990).
[50] A. Amon, A. Mikhailovskaya, and J. Crassous, Spatially resolved measurements of micro-deformations in granular materials using diffusing wave spectroscopy, Rev. Sci. Instrum. **88,** 051804 (2017).
[51] H.M. van der Kooij, S. Dussi, G.T. van de Kerkhof, R.A. Frijns, J. van der Gucht, and J. Sprakel, Laser Speckle Strain Imaging reveals the origin of delayed fracture in a soft solid, Sci. Adv. **4,** eaar1926 (2018).
[52] H.M. van der Kooij, A. Susa, S.J. Garcia, S. van der Zwaag, and J. Sprakel, Imaging the Molecular Motions of Autonomous Repair in a Self-Healing Polymer, Adv. Mater. **29,** (2017).
[53] T. Verho, P. Karppinen, A.H. Groschel, and O. Ikkala, Imaging Inelastic Fracture Processes in Biomimetic Nanocomposites and Nacre by Laser Speckle for Better Toughness, Adv. Sci. (Weinh) **5,** 1700635 (2018).
[54] D.J. Durian, Accuracy of diffusing-wave spectroscopy theories, Phys. Rev. E **51,** 3350 (1995).
[55] S. Lynch, *Image Processing with Python, Dynamical Systems with Applications using Python* (Springer, 2018), p. 471.
[56] C.R. Harris, K.J. Millman, S.J. van der Walt, R. Gommers, P. Virtanen, D. Cournapeau, E. Wieser, J. Taylor, S. Berg, and N.J. Smith, Array programming with NumPy, Nature **585,** 357 (2020).
[57] H. Tanaka, T. Hayashi, and T. Nishi, Digital image analysis of droplet patterns in polymer systems: point pattern, J. Appl. Phys. **65,** 4480 (1989).